Quarterly Report for

July - September 2000

Stanford Geothermal Program

DE-FG07-99ID13763

Table of Contents

1. MEASUREMENTS OF STEAM-WATER RELATIVE PERMEABILITY

This research project is being conducted by Research Assistant Peter O'Connor and Professor Roland Horne. The aim is to measure relative permeability relations for steam and water flowing simultaneously in rock and to examine the effects of temperature, flow rate, and rock type. In the first stage, the experiments will attempt to reproduce results obtained in a previous experiment (Mahiya, 1999), but holding the experimental pressure as close as possible to a constant value.

1.1 BACKGROUND

An X-ray CT technique has been used in recent years to measure the distribution of steam and water saturation in rocks to obtain steam-water relative permeability curves (Satik, 1998, Mahiya, 1999).

The current experiment is attempting to maintain a constant pressure, to avoid complications of the slip factor. As the experiment will be constantly at an inlet gauge pressure of 15 psi, it will necessarily be at a constant 120ºC at the inlet in order to have two-phase flow throughout, with the rest of the core being at the saturation temperature for the pressure at that point. Our expectation is an identical pressure profile and temperature profile for every step of the process.

1.2 EXPERIMENTAL PROCEDURE

A Berea sandstone was drained, flushed with nitrogen, then subjected to a vacuum. A dry X-ray scan was made to obtain CT_{dry}. The next step was to saturate the core with water and scan to obtain CT_{wet}; however, the CT scanner failed at this point and this step will have to be repeated. From these scans, a porosity distribution will be obtained, expected to yield an average value of 24.7%. In the next step, hot liquid water is flowed through to obtain CT_{hw}, which is necessary to calculate experimental saturations. The next steps are the actual flow-through experiments. The core will be under a pressure gradient of approximately 15 psi across the 41-cm length. First, the core is saturated with steam. Steam flow rate will be gradually lowered in 10% increments, to implement an imbibition process whereby the wetting phase (water) displaces the nonwetting phase (steam). A flexible heat guard ensures negligible overall heat loss for a near-adiabatic process. The flexible heat guard control mechanism was re-designed this year. At each step, the system will reach a steady state and will then be subject to CT scan to measure saturation. Steam flow rate will be reduced to 0%, then increased. This second sequence will be a drainage sequence.

At every stage, pressure, temperature and heat fluxes from the core are to be measured. Calculated relative permeability to steam and water are then plotted against the saturation measurements. The major suggested change from the previous experiment is to perform the imbibition step first. Performing the imbibition step first allows determination of the maximum pressure. This pressure can be maintained by increasing flow rates if

necessary.

In the spring quarter, we worked to determine the correct flow rates and power inputs to ensure a pressure differential of 15 psi and a temperature at the inlet of slightly over 120º C for the steam, and slightly under 120º C for the hot water. In this procedure, we determined several pairs of flow rates for water and steam, at different ratios, to result in steady-state flow with a pressure differential of 15 psi. This process also determined the corresponding voltage and current settings for the hot water and steam heaters and for the flexible heater. All that is unknown is the saturation; once the CT scanner is available, it should be a simple matter to determine the saturation. However, the core was damaged through excessive heat in the process, and we are currently awaiting replacement parts.

1.3 FUTURE RESEARCH

Future research will involve repeating the experiment at different pressure gradients and temperatures. The next experiment will probably occur at approximately half the current pressure gradient. In each case, the experiment will maintain a uniform pressure gradient for the range of saturations.

Also under consideration are other possible methods of measuring saturation, either by weighing the core or using acoustic sounding to determine saturation. While not as precise as the CT scanner, these methods have the advantage of producing average saturation readings extremely quickly.

Basic calculations show that a water-saturated core at 120º C would weigh 0.2 kg more than a steam-saturated core. Such a difference is great enough to allow for measurement of the whole range of saturations; however, it would require the assumption of uniform saturation throughout the core. The presence of a steam front would not be detected by simply weighing the core.

Acoustic sounding would use the travel time for a sound wave signal to determine the saturation of the core. Several sensors could be placed, to determine saturations at many locations simultaneously. Saturation-sound speed relations could be calculated theoretically using the Gassman relations or could be calibrated using the CT scanner. More research will be necessary on the effects of geometry on the method; it may be that a rectangular core would be better suited to this method.

2. STEAM-WATER CAPILLARY PRESSURE

This research project is being conducted by Research Associate Kewen Li and Professor Roland Horne. In this study the imbibition steam-water capillary pressures were measured by using an X-ray CT technique and compared to the imbibition air-water capillary pressures in the same ceramic core sample. The final objective of this project is to develop new techniques of measuring and calculating steam-water capillary pressure in geothermal systems.

2.1 SUMMARY

Steam-water flow exists in all two-phase geothermal reservoirs. Steam-water capillary pressure plays important role in controlling fluid distribution, well productivity, and ultimate reserves. However, it is very difficult to measure steam-water capillary pressure. Are there any differences between steam- and air-water capillary pressures? If not, we could represent steam-water flow by air-water flow, which would be a major advantage since air-water capillary pressure can be measured easily. To this end, we conducted spontaneous water imbibition experiments using the same core sample saturated first with steam and then a second time with air. The imbibition steam- and air-water capillary pressures in the core sample were measured using an X-ray CT technique. The results were compared, and it was found that there are significant differences between steam- and air-water capillary pressures. The imbibition steam-water capillary pressure was less than the air-water capillary pressure.

2.2 INTRODUCTION

Li and Horne (2000a) described a method to measure and calculate steam-water capillary pressure due to the experimental evidence of significant differences between steam- and air-water flow shown by Horne et al. (2000). However, there have been no investigations showing the direct comparison between steam-water capillary pressure and air-water capillary pressure in the same core sample. In order to identify the differences between the two, we conducted spontaneous water imbibition (cocurrent) experiments into the same core sample saturated with steam and with air. The core sample was positioned vertically. The steam- and air-water capillary pressures were calculated using the relationship between height and water saturation measured by the X-ray CT method after the equilibrium between gravity and capillary pressure had been reached.

2.3 THEORY

In this study, the basic theory behind the measurement of steam- and air-water capillary pressures is the balance between gravity and capillary pressure as a function of height in a core sample positioned vertically. Steam-water or air-water capillary pressure is equal to the gravity force once the spontaneous water imbibition into the core sample has been completed. The equation is expressed as follows:

$$P_{ci} = \Delta\rho g h \qquad (2.1)$$

where P_{ci} is steam-water or air-water capillary pressure; $\Delta\rho$ is the density difference between water and steam or air; g is gravity constant and h the height. The water saturation in the core at h was measured by using an X-ray CT method. Water saturation is calculated as follows:

$$S_w = \frac{CT_{\exp}(T) - CT_{dry}(T)}{CT_{wet}(T) - CT_{dry}(T)} \tag{2.2}$$

where $CT_{wet}(T)$, $CT_{dry}(T)$ are CT numbers of the core when it is fully saturated by water and air respectively; $CT_{exp}(T)$ is the CT number of the rock when it is partially saturated by steam, all at the same temperature T.

Porosity is usually computed using the following expression:

$$\phi = \frac{CT_{wet}(T) - CT_{dry}(T)}{CT_{water}(T) - CT_{air}(T)} \tag{2.3}$$

where CT_{water} and CT_{air} are the CT numbers of water and air respectively. However, the ceramic core sample used in this study had a hollow center, as shown in Figure 2.1. Hence we used a modified equation to calculate the porosity of the core sample with this particular shape once we know the CT values of the whole area with a radius of r_o.

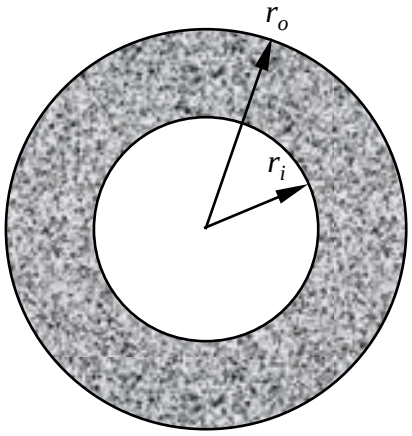

Figure 2.1: Cross-section of the ceramic core sample.

The CT values, $CT_{wet}(T)$ and $CT_{dry}(T)$, of the whole area with a radius of r_o can be measured. The porosity calculated using Eq. 2.3 is the mean porosity ϕ_m in that area, including the hole. The mean porosity is expressed as follows:

$$\phi^m = \frac{CT^m{}_{wet}(T) - CT^m{}_{dry}(T)}{CT_{water}(T) - CT_{air}(T)} \tag{2.4}$$

where $CT^{m}{}_{wet}(T)$ and $CT^{m}_{dry}(T)$ are the average CT values of the whole area with a radius of r_o when the sample is saturated with water and air, respectively. If we know the CT values of the rock part, then the porosity can be calculated using the following equation:

$$\phi = \frac{CT^{o}{}_{wet}(T) - CT^{o}{}_{dry}(T)}{CT_{water}(T) - CT_{air}(T)} \tag{2.5}$$

where $CT^{o}{}_{wet}(T)$ and $CT^{o}_{dry}(T)$ are the average CT values of the annular area between r_o and r_i (see Figure 2.1) when the sample is saturated with water and air, respectively. We can measure $CT^{m}{}_{wet}(T)$ and $CT^{m}_{dry}(T)$ easily. Therefore, the question is how to calculate $CT^{o}{}_{wet}(T)$ and $CT^{o}_{dry}(T)$ from the measured values of $CT^{m}{}_{wet}(T)$ and $CT^{m}_{dry}(T)$. To this end, it is necessary to look into the fundamentals of the X-ray CT method. The linear absorption coefficient of X-ray through a uniform object is equal to:

$$\mu = \mu_m \rho \tag{2.6}$$

where μ and μ_m are the linear absorption coefficient and mass absorption coefficient; ρ is the density of the object. For a nonuniform object composed of n components, the following equation applies:

$$\mu = \sum_{i=1}^{n} \mu_i V_i \tag{2.7}$$

where μ_i and V_i are the linear absorption coefficient and the volumetric fraction of component i.

The CT value is defined as follows:

$$CT = 1000 \frac{\mu - \mu_w}{\mu_w} \tag{2.8}$$

where μ_w is the linear absorption coefficient of pure water. The CT value of water should be equal to zero according to Eq. 2.8 but the actual measurements may shift from zero due to the calibration error or other reasons. The absorption of X-ray in air is very small, so the CT value of air should be around –1000. The measured value of CT_{air} in this study was –1005.

According to Eqs. 2.7 and 2.8, the CT value of a nonuniform object can be calculated as follows:

$$CT = \sum_{i=1}^{n} CT_i V_i \tag{2.9}$$

where CT_i is the CT value of component i.

The object shown in Figure 2.1 can be considered as two parts: the hole and the annular solid. According to Eq. 2.9, the following expressions apply:

$$CT_{wet}^{m} = CT_{wet}^{o} \frac{A_r}{A_m} + CT_{wet}^{h} \frac{A_h}{A_m} \tag{2.10}$$

where CT^{h}_{wet} is the CT value of the hole when the core sample is saturated with water. A_r, A_h and A_m are the areas of the annular part between r_o and r_i, the hole and the whole object (see Figure 2.1).

$$CT_{dry}^{m} = CT_{dry}^{o} \frac{A_r}{A_m} + CT_{dry}^{h} \frac{A_h}{A_m} \tag{2.11}$$

here CT^{h}_{dry} is the CT value of the hole when the core sample is saturated with air or steam. In our experiment, no water existed in the hole when the core sample was saturated with water. Therefore, CT^{h}_{dry} is equal to CT^{h}_{wet} in this case. Using Eqs. 2.10 and 2.11, we can obtain:

$$(CT_{wet}^{o} - CT_{dry}^{o}) = \frac{A_m}{A_r}(CT_{wet}^{m} - CT_{dry}^{m}) \tag{2.12}$$

Substituting Eq. 2.12 into Eq. 2.5:

$$\phi = \frac{A_m}{A_r} \frac{CT_{wet}^{m} - CT_{dry}^{m}}{CT_{water} - CT_{air}} \tag{2.13}$$

Substituting Eq. 2.4 into Eq. 2.13:

$$\phi = \frac{A_m}{A_r} \phi_m \tag{2.14}$$

Eq. 2.14 can also be expressed as follows:

$$\phi = \frac{r_o^2}{r_o^2 - r_i^2}\phi_m \tag{2.15}$$

The inner radius r_i and the outer radius r_o are known. Therefore, the porosity of the core sample as shown in Figure 2.1 can be calculated using Eq. 2.15 once the average porosity is measured.

Using a similar procedure, we were able to prove that the water saturation in the annular part, S_w, is equal to the average water saturation, S_{wm}, in the whole area. Therefore, we could calculate water saturation in the core sample using Eq. 2.2 with all the CT values from the whole object.

2.4 EXPERIMENTS

Rock and Fluids. Distilled water was used as the liquid phase in this study; the specific gravity and viscosity were 1.0 and 1.0 cp at 20°C. Steam and air were used as the gas phase; the surface tension of water/air at 20°C was 72.75 dynes/cm. The values of the surface tension at high temperatures were calculated from the steam property software from Techware Engineering Applications, Inc. It was assumed, as usual, that there were no differences between the surface tension of water/air and that of water/steam. The ceramic sample was provided by Refractron Technologies Corp. and had a porosity of 39.19%, a length of 25.0 cm, an inner diameter of 4.275 cm, and an outer diameter of 6.287 cm. We did not measure the permeability of the core sample yet due to its special shape but the permeability was estimated to be more than 10 darcy.

X-ray CT Scanner. Distribution of water saturation in the core sample was measured along the height using a Picker™ Synerview X-ray CT scanner (Model 1200 SX) with 1200 fixed detectors. The voxel dimension was 0.5 mm by 0.5 mm by 5 mm, the tube current used was 50 mA, and the energy level of the radiation was 140 keV. The acquisition time of one image was about 3 seconds while the processing time was around 40 seconds.

Experimental Apparatus. A schematic of the apparatus is shown in Figure 2.2. The core system was assembled in an aluminum cylinder wrapped in a heating belt; the temperature in the cylinder was controlled using an Autotune Temperature Controller (manufactured by OMEGA, Model CN6071A) by turning the heating belt on and off automatically. The temperatures at both the top (in steam or air) and the bottom (in water) of the core were measured during the experiment. A simulation test was conducted before the entire system was assembled in the CT scanner in order to obtain uniform temperature distribution along the core. We wanted to have the temperature at the top, T_1, equal to that at the bottom, T_2 (See Figure 2.2). This was realized by adjusting the spacing between two strips of the heating belt wrapped outside the aluminum cylinder.

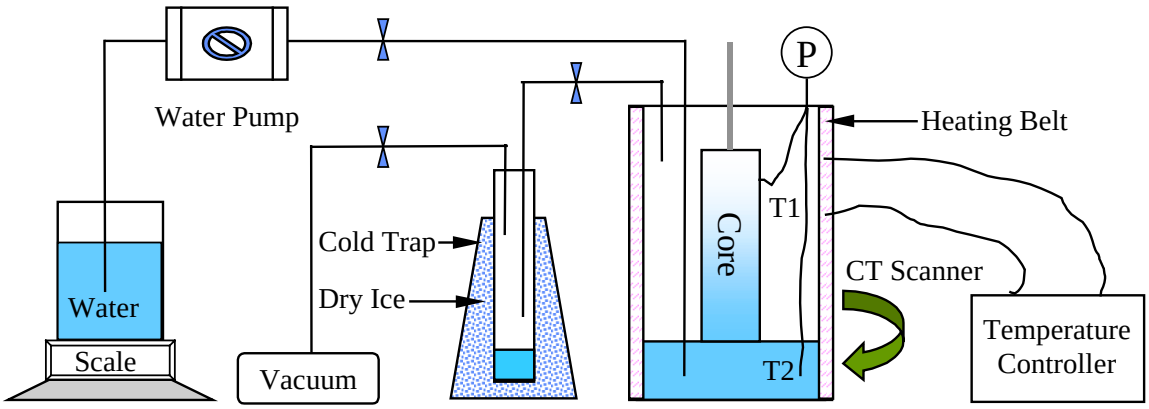

Figure 2.2: Schematic of the apparatus of measuring steam- and air-water capillary pressure.

The vacuum pump (Welch Technology, Inc., Model 8915) was used to remove the air in the core sample and in the aluminum cylinder. The cold trap with dry ice was employed to protect the steam from entering the vacuum pump in order to extend its life and reduce the frequency of replacing the pump oil. Water in the aluminum cylinder was delivered by the water pump (Dynamax, Model SD-200), manufactured by RAININ Instrument Co., and the amount was measured by the scale (Mettler, Model PE 1600) with an accuracy of 0.01g and a range from 0 to 1600g. Comparing the volume of the space under the bottom of the core, which was known, we could judge whether the water contacted the bottom of the core sample or not. This judgement was aided by the CT scanning near the bottom. We kept scanning from time to time and could know where the water level was by checking the CT values in the annular space.

Procedure. The core sample was dried by heating to a temperature of 105^{o}C until the weight did not vary during 8 hours or more. We conducted the spontaneous water imbibition into the air-saturated and upward-positioned core sample using the procedure of Li and Horne (2000b) at room temperature. An X-ray CT scan was made at each centimeter along the sample before and after the water imbibition. Then the core was dried again and saturated with water. Another X-ray CT scan was made after the saturation to obtain the values of CT_{wet}. We calculated the air-water capillary pressure in the core sample using these measurements.

The core sample was dried one more time and was assembled in the aluminum cylinder (see Figure 2.2). One X-ray CT scan was made to obtain the values of CT_{dry} since these may be affected by the presence of the aluminum cylinder. After that, the temperature of the core system was increased to about 98^{o}C. We scanned the core to obtain the values of CT_{dry} at 98^{o}C about 10 hours later after the core was kept at this temperature. The main purpose of waiting 10 hours was to obtain a uniform temperature distribution. The core was evacuated to 60 minitorr for about 4 hours to remove the air in the core after the hot scan. A certain amount of water was then introduced into the bottom of the aluminum cylinder using the water pump. The core then became saturated with steam. Water started to imbibe into the steam-saturated core once the bottom of the sample was brought into

contact with the water surface that was raised by injection using the water pump. In order to monitor the distribution of water saturation in the core sample, we scanned the core from time to time until the imbibition of water was completed. Finally, the sample was dried again and the last X-ray CT scan was made after completely resaturating with water. The CT values measured under different states were used to calculate the porosity by Eqs. 2.4 and 2.15. Also calculated was the distribution of the water saturation as a function of height using Eq. 2.1. We obtained the steam-water capillary pressure from these data.

2.5 RESULTS

We conducted spontaneous water imbibition into both steam- and air-saturated core sample to compute steam- and air-water capillary pressures. Figure 2.3 shows the CT values of the whole area with a radius of r_o (see Figure 2.1) when the core was dry and saturated with water.

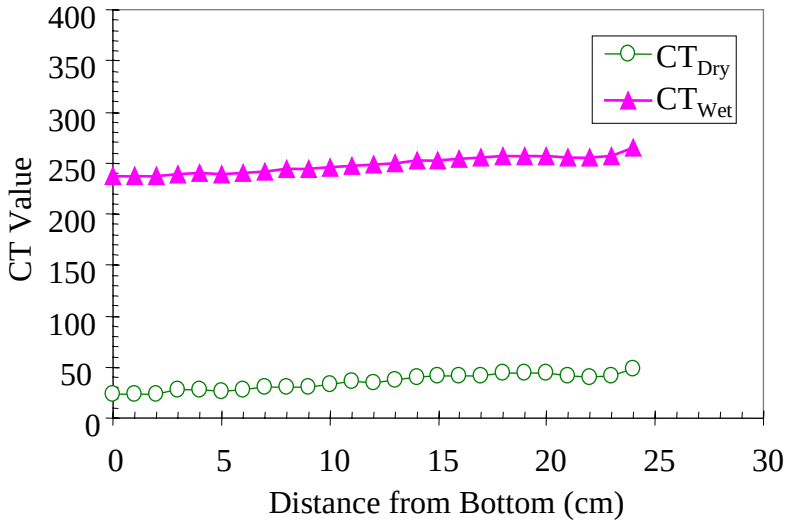

Figure 2.3: Distribution of CT value in the core sample.

The porosity of the core sample was calculated using Eqs. 2.4 and 2.15, as shown in Figure 2.4. The porosity distribution along the height of this ceramic core sample was very homogeneous and its average value was 39.61%. The porosity measured using the saturation method was 39.19%, close to the value of 39.61% obtained from the X-ray CT method. The average porosity calculated using Eq. 2.3 (including the hole) is also shown in Figure 2.4; as expected, it is much smaller than those values of the actual porosity.

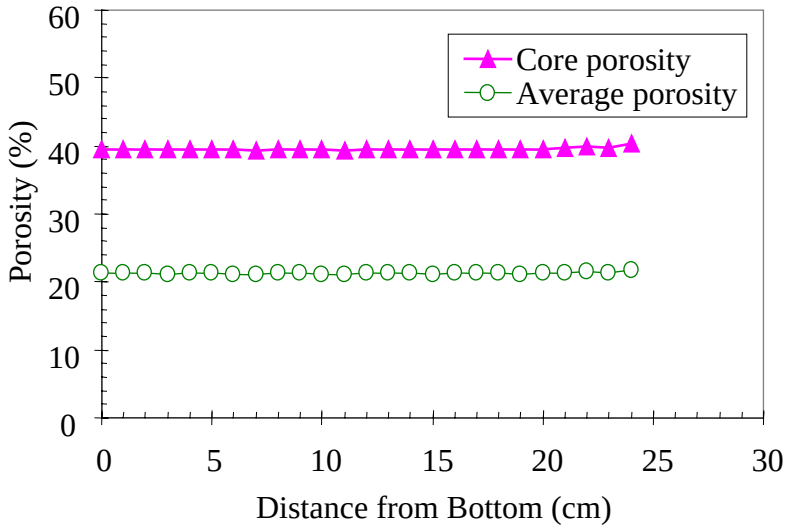

Figure 2.4: Porosity distribution of the core sample.

Using the image manipulation tools provided in the X-ray CT machine, we could measure the CT value of a local area of any size in the CT image. We measured the CT values of four circular areas (top, bottom, left, and right sides) in the annular part of the core sample between r_o and r_i at different states. Then we calculated the mean values of the CT numbers from the four different areas for each state (dry, wet, and after water imbibition). The calculated results of the core sample before and after the spontaneous water imbibition, including those when the core was saturated completely with water, are shown in Figure 2.5. Obviously, the values of CT_{dry} and CT_{wet} shown in Figure 2.5 are different from those in Figure 2.3. This is because the calculated CT numbers using this method are the real CT values of the core instead of those (in Figure 2.3) including the empty hole in the center. With the CT values shown in Figure 2.5, we also calculated the porosity of the core sample by using Eq. 2.3 directly instead of Eq. 2.15. The average porosity calculated using the data shown in Figure 2.5 is also 39.61%, the same as that in Figure 2.4. This confirms the validity of calculating porosity using Eq. 2.15. The method of measuring average CT values as shown in Figure 2.5 is much more time-consuming than measuring those shown in Figure 2.3. Therefore, for all the rest of calculation, we only measured the CT values for the whole area with a radius of r_o (see Figure 2.1).

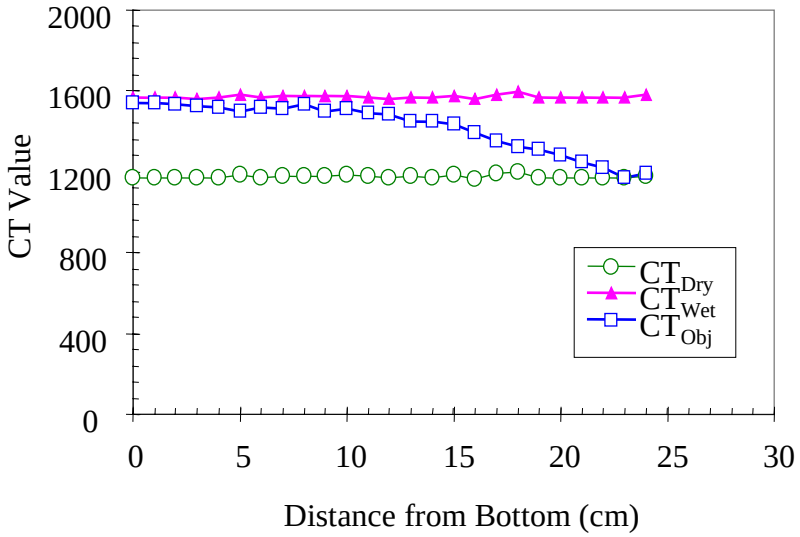

Figure 2.5: CT distribution before and after water imbibition in the air-saturated core (including those for complete saturation with water).

Using the data in Figure 2.5, the air-water capillary pressure of the core sample at a temperature of 21°C was calculated and is plotted in Figure 2.6.

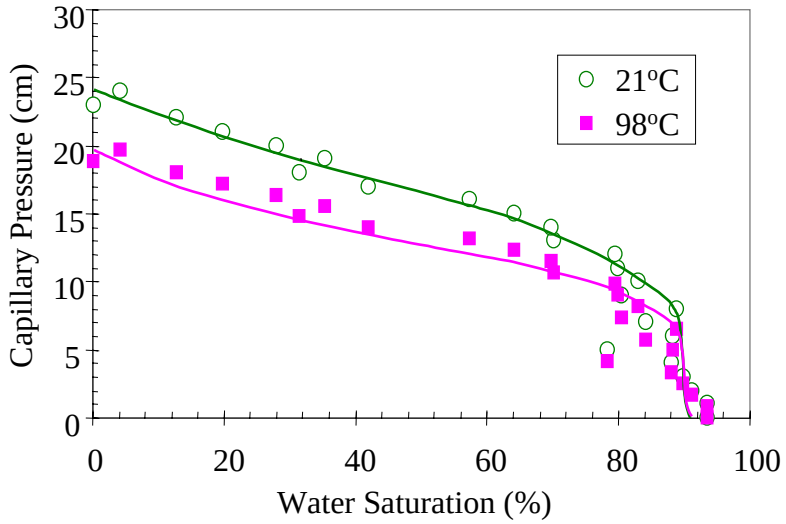

Figure 2.6: Air-water capillary pressure curves.

Steam-water capillary pressure was measured at a temperature of 98°C and a pressure lower than the atmosphere pressure. Therefore we needed to scale the air-water capillary pressure data at 21°C to 98°C in order to compare steam- and air-water capillary pressure curves in the same core sample. Assuming that there is no effect of temperature on the wettability or contact angle of the fluid-rock system, the air-water capillary pressure at a temperature of T_2 can be calculated from that at a temperature of T_1 using the following equation (Li and Horne, 2000c):

$$P_c^{T_2}(S_w) = \frac{\sigma_{T_2}}{\sigma_{T_1}} P_c^{T_1}(S_w) \tag{2.16}$$

where $P_c^{T_1}(S_w)$ and $P_c^{T_2}(S_w)$ are the air-water capillary pressure at the same water saturation of S_w but at different temperatures of T_1 and T_2. The air-water capillary pressure at a temperature of 98°C calculated using Eq. 2.16 is shown in Figure 2.6.

We measured the distribution of the water saturation along the height from time to time after starting the spontaneous water imbibition into the steam-saturated core sample. The relationships between the height and the water saturation at different time of water imbibition are demonstrated in Figure 2.7. It can be seen that the water imbibition stopped at about 24 hours. This implies that the capillary and gravity forces were in equilibrium by this time. The steam-water capillary pressure could be calculated according to the force balance (considering the height as the capillary pressure).

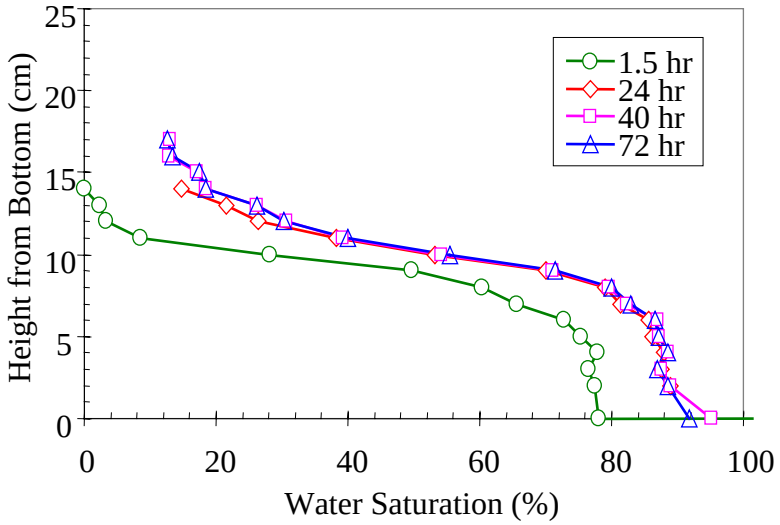

Figure 2.7: Distribution of water saturation in the core at different time at a temperature of 98°C.

The calculated steam-water capillary pressure at 98°C is plotted in Figure 2.8. Air-water capillary pressure scaled previously to the same temperature is also shown in Figure 2.8 for comparison. The experimental results demonstrate that steam-water capillary pressure in the ceramic core is less than the air-water capillary pressure at the same water saturation. The differences between the two are significant. However, there are almost no differences between the residual steam saturation and the residual air saturation as shown in Figure 2.8. Horne et al. (2000) observed that the residual steam saturation was less than the residual nitrogen saturation in Berea sandstone with a permeability of about 1400 md, which was much lower than the permeability of the ceramic core in this study. We may need more research on this issue.

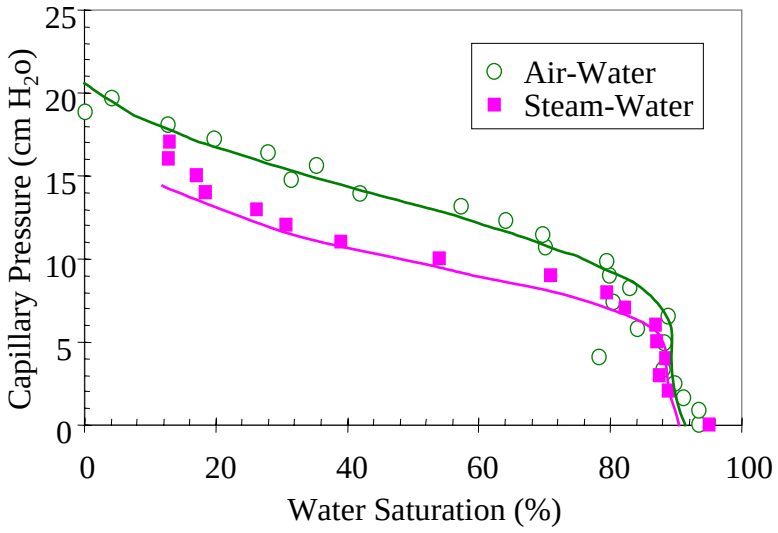

Figure 2.8: Comparison of steam- and air-water capillary pressure curves at a temperature of 98^{o}C.

Few reports could be found regarding the comparison between steam- and air-water capillary pressures. In order to confirm the phenomenon we observed in Figure 2.8, we are planning to conduct water drainage tests in the same core but under different conditions (steam- and air-saturated). In doing this we will obtain drainage steam- and air-water capillary pressures.

2.6 CONCLUSIONS

Based on the present work, the following conclusions may be drawn:

1. A direct method of measuring steam-water capillary pressure in geothermal systems has been developed based on an X-ray CT technique.
2. Imbibition steam-water capillary pressure in the ceramic core sample studied is less than the imbibition air-water capillary pressure at the same water saturation. The differences between the two are significant.
3. The experimental results in this study show that we may not be able to infer steam-water flow measurements simply using air-water experiments.

2.7 FUTURE WORK

The next step is to measure the drainage steam- and air-water capillary pressures using the same rock sample in order to identify the differences between them.

3. WATER INJECTION

This research project is being conducted by Research Associate Kewen Li, Huda Nassori, and Professor Roland Horne. Water injection has been investigated at different pore pressures and temperatures. The objective of this project is to study the effects of temperature and pressure on the in-situ water saturation and the end-point relative permeability in a core sample.

3.1 SUMMARY

Water injection has been proved a successful engineering technique in geothermal reservoirs, such as The Geysers, as a means to maintain reservoir pressure and sustain well productivity. However, many questions related to water injection into geothermal reservoirs still remain unclear. For example, how does the in-situ water saturation change with reservoir pressure and temperature? How does the reservoir pressure influence well productivity? To answer these questions, we studied the effects of temperature and pressure on the in-situ water saturation in a core sample using an apparatus developed for this work. The in-situ water saturation decreases very rapidly once the saturation pressure is reached. When the mean pressure in the core sample decreases further, the in-situ water saturation decreases sharply again to almost zero at a pressure much less than the saturation pressure. Also investigated were the effects of pressure on well productivity index. We found that well productivity first increased with the increase of mean reservoir pressure within a certain range but then decreased. The well productivity reached a maximum value at a pressure close to the saturation pressure. Using the same apparatus, we also measured the end-point steam relative permeabilities.

3.2 INTRODUCTION

In order to answer the questions related to water injection, it is necessary to measure fluid saturation in the expriements. However, it is difficult to measure steam or water saturation in a geothermal core sample due to the significant mass transfer and phase transformation between steam and water phases. In the past, we have measured the steam or water saturation and their distribution using an X-ray CT technique. This method is accurate and fast but it is complicated, expensive, and sometimes not available because of maintenance of the instrument or other nontechnical reasons. Therefore, we developed an alternative method and designed an apparatus to infer the average steam or water saturation by weight measurements. Using this approach we were able to measure the average in-situ water saturation and the end-point relative permeability. We also studied the effects of temperature and pressure on the in-situ water saturation.

3.3 MATHEMATICS

Although we did not measure water saturation using the X-ray CT technique, we did use the CT approach to measure the porosity distribution of the core sample. Another purpose in using the X-ray CT machine was to determine whether the core sample and the core holder had any fractures since the core system, including the core sample and holder, had been used before at high temperatures.

Porosity is computed using the following expression:

$$\phi = \frac{CT_{wet}(T) - CT_{dry}(T)}{CT_{water}(T) - CT_{air}(T)} \tag{3.1}$$

where $CT_{wet}(T)$, $CT_{dry}(T)$ are CT numbers of the rock when it is fully saturated by water and air at a temperature of T, respectively; $CT_{water}(T)$ and $CT_{air}(T)$ are the CT numbers of water and air at a temperature of T.

Productivity index is calculated as follows:

$$PI = \frac{q}{\Delta p} \tag{3.2}$$

here PI is the productivity index; q is the production at the outlet of the core sample and Δp the differential pressure across the core sample.

3.4 EXPERIMENTS

Rock and Fluids. Distilled water was injected into the core as the liquid phase; the specific gravity and viscosity were 1.0 and 1.0 cp at 20°C. The surface tension of water/steam at 20°C is 72.75 dynes/cm. The values of the surface tension at high temperatures were calculated from the steam property software bought from Techware Engineering Applications, Inc. A Berea sandstone sample fired at high temperature was used; its permeability and porosity were 1440 md and 25.0%; the length and diameter were 43.2 cm and 5.08 cm, respectively.

Experimental Apparatus. A schematic of the apparatus is shown in Figure 3.1. The steam generator was a heater with a power of 500 W. The power required to generate steam was calculated roughly according to the flow rate of water injection and the temperatures of water and steam. To ensure that the injected cold water was evaporated fully to steam, a coil of stainless steel tubing with a length of about 2 m was installed between the steam generator and the inlet of the core in the oven. A thermocouple was installed in the water injection line close to the inlet of the core sample in order to measure the temperature (T_1) of the fluid injected into the core. Another thermocouple was installed to measure the temperature (T_2) in the oven but around the core system. The flow parameters were not measured until T_1 was equal to T_2. The balance (Model BP6100) in Figure 3.1 was manufactured by Sartorius Corporations and used to monitor the water saturation in the core sample; this balance has an accuracy of 0.1g and a range from 0 to 6100 g.

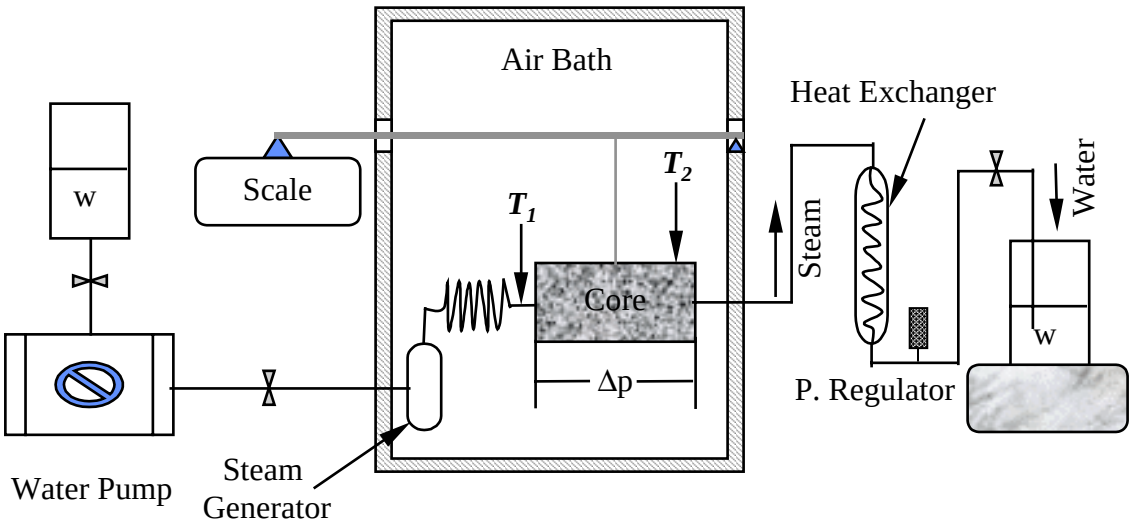

Figure 3.1: Schematic of the apparatus.

The pump (Model III) used to inject distilled water was manufactured by ConstaMetric; the minimum flow rate is 0.1 ml/min with an accuracy of 1%. This pump is a constant-rate pump; its flow rate was calibrated before the experiment. The calibration was done by using a stop watch and a Mettler balance (Model PE 1600) with an accuracy of 0.01g and a range from 0 to 1600 g. The flow rate of this pump at room temperature is shown in Figure 3.2. The measured flow rates were consistent with those specified on the pump.

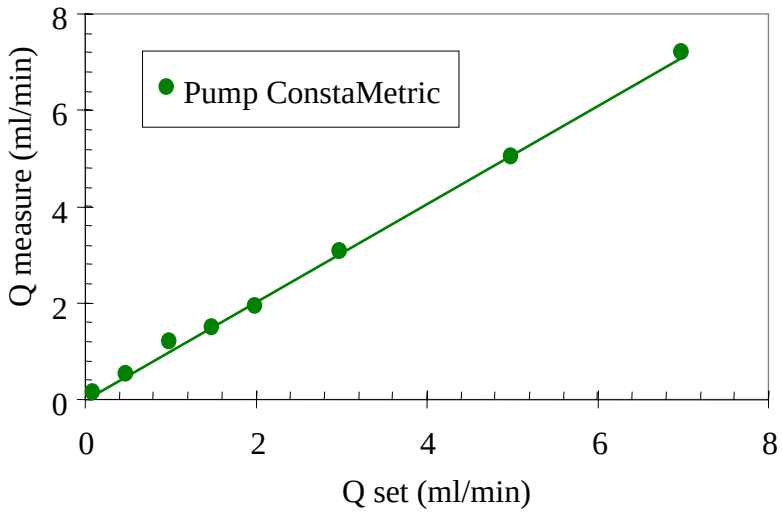

Figure 3.2: Calibration of flow rate for the water pump.

The flow rate of steam can be calculated using the water injection rate and the density of steam at the temperature and pressure measured during the experiment.

Procedure. The core sample was dried by heating to a temperature of 105^{o}C until the weight did not vary during eight hours or more. The porosity and its distribution were measured using the X-ray CT method after the core system was cooled. The core sample was then saturated with distilled water and the core system was assembled in the apparatus shown in Figure 3.1. The absolute permeabilities were measured at different flow rates and different pore pressures. The purpose was to confirm that the core was completely saturated with water and to detect any other abnormal phenomena. For example, if there were significant amount of air in the core sample, the permeability might change with the flow rates. Following that, the temperature in the oven was raised to 110^{o}C while the pressure at the outlet of the core sample was increased to 35 psia, (which is above the saturation pressure at this temperature) using the back pressure regulator installed outside the oven. We measured the permeability at a temperature of 110^{o}C 24 hours later to make sure that the permeability was equal to that measured at low temperature. After that, the pressure at the outlet was decreased gradually to atmospheric pressure while the temperature was kept constant and the water was injected continuously into the core. This was the first drainage process at variable mean pressure. The first imbibition process was conducted by increasing the pressure at the outlet. The change of the reading from the balance and the differential pressure across the core sample were recorded during both the drainage and the imbibition processes. Using a similar procedure, we conducted a second drainage test by varying the system temperature to study the effect of temperature on the in-situ water saturation.

3.5 RESULTS

The core system did not sit on the scale directly. Therefore the weight variation recorded by the scale was not that of the actual core system but was related to it linearly. To find the relationship between the weight measured by the scale and that of the core system, we used standard known weights to substitute the core system. We could obtain the reading recorded by the scale for different weights. The relationship between the two is shown in Figure 3.3. The weight of the core system can be calculated from the reading of the scale using the relationship as follows:

$$W_{core} = 3.4W_{scale} - 0.095 \tag{3.3}$$

where W_{core} and W_{scale} are the weight of the core and the reading of the scale, respectively.

We found that the relationship represented by Eq. 3.3 was somewhat temperature-dependent. So the scale was calibrated at both room temperature and high temperature. The relationship in Eq. 3.3 represents the calibration at a temperature of 110^{o}C. Most of the experiments were conducted at this temperature.

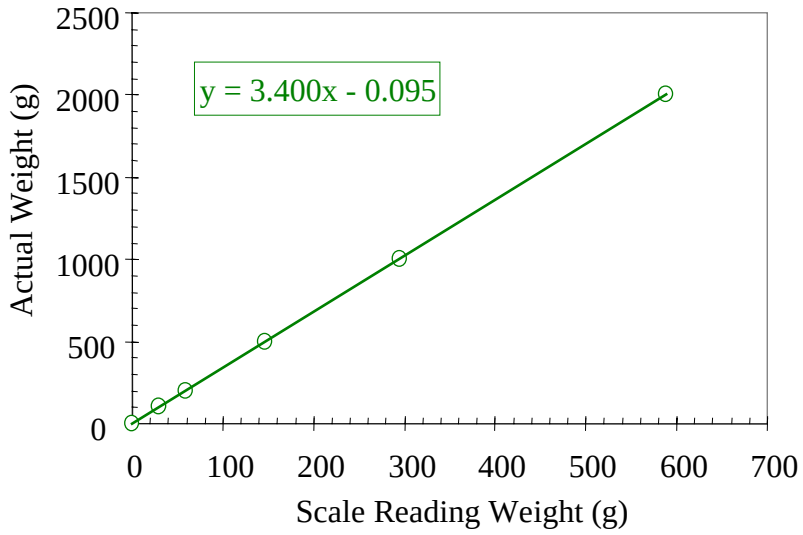

Figure 3.3: Calibration of the scale at 110^{o}C.

The pressure transducer was also calibrated using a pressure gauge with an accuracy of 0.05 psi. The calibration curve is shown in Figure 3.4.

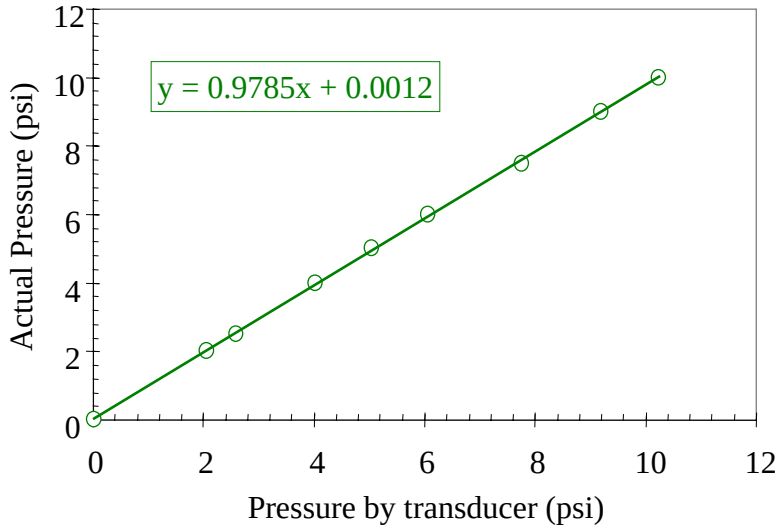

Figure 3.4: Calibration of pressure transducer.

Figure 3.5 shows the CT values at different positions in the core sample when it was dry and saturated with water.

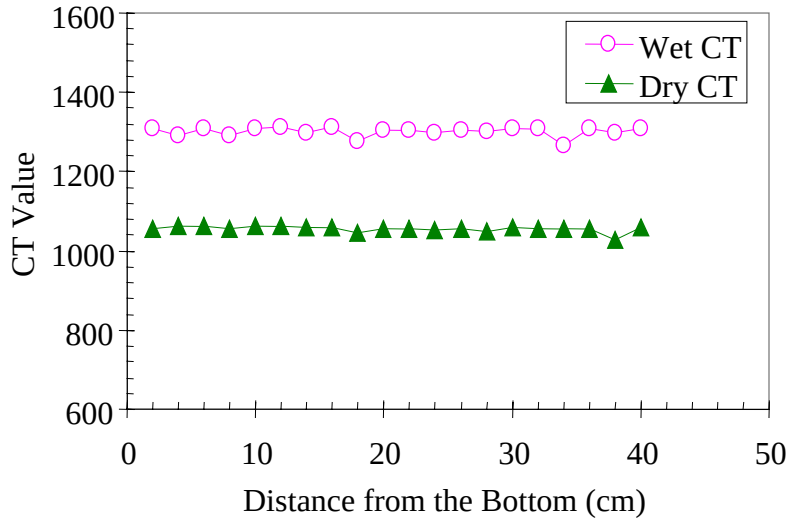

Figure 3.5: CT distribution before and after water saturation.

Using the data in Figure 3.5, the porosity and its distribution of the core sample were calculated with Eq. 3.1 and are plotted in Figure 3.6. The average porosity measured using the X-ray CT technique was about 24.75%; the porosity measured using the wet vs. dry weight method was about 25.0%. The two values of the porosity using different methods are in good agreement. We did not see any visible fractures in the core sample in the CT images.

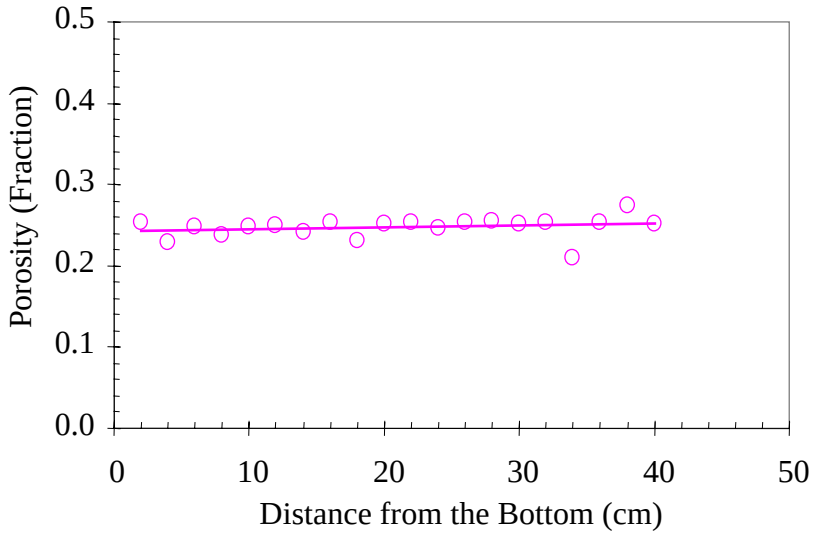

Figure 3.6: Porosity and its distribution of the core sample.

After the core was saturated with water, the permeability was measured at different flow rates with and without back pressure applied. The results are shown in Figure 3.7. The variation of permeability at different flow rates was negligible. The fact that the

permeability was almost constant at different flow rates and different mean pore pressure demonstrated that the core sample was completely saturated with water.

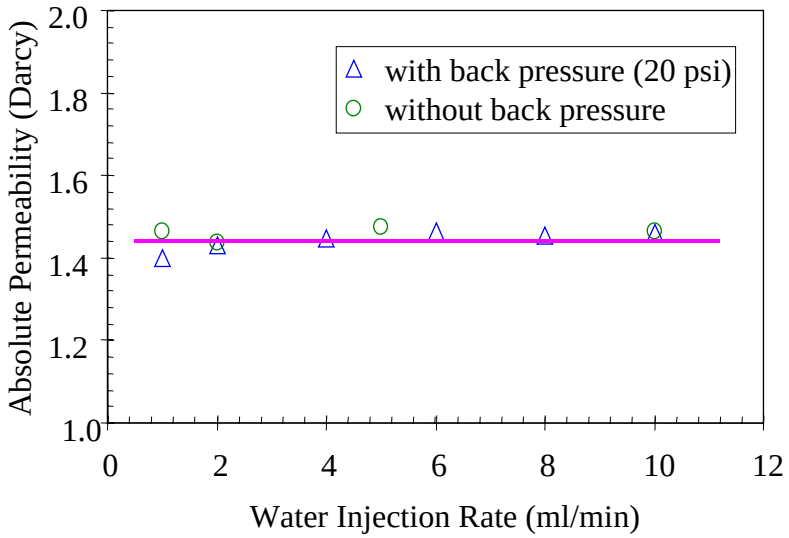

Figure 3.7: Permeability of the core at different flow rates and mean pressures.

The temperature of the core system was raised to 110^{o}C while the outlet pressure was kept at 35 psia and the water injection rate was kept at 0.5 ml/min. Then the pressure at the outlet of the core sample was decreased step by step. The in-situ water saturation in the core sample was calculated using the data from the scale with calibration relationship of Eq. 3.2. The computed results are shown in Figure 3.8. The mean pore pressure in the core sample was calculated using the outlet pressure and the differential pressure across the core. The in-situ water saturation decreases with the decrease of the mean pore pressure and drops very sharply close to the saturation pressure at this temperature, which is 20.8 psia. Interestingly, the water saturation did not drop to zero, but to about 40 percent. This may be due to the effect of adsorption. When the mean pore pressure decreases further, the in-situ water saturation decreases abruptly again, to almost zero. The core dried out. The drainage curve of in-situ water saturation vs. mean pore pressure is characteristic of a two-step decrease (see Figure 3.8). Following the drainage process, we increased the mean pore pressure gradually while the injection rate of water was kept at the same value, 0.5 ml/minute. Figure 3.8 shows that the in-situ water saturation increases with the increase of the mean pore pressure and increases sharply close to the saturation pressure. However, we did not observe the second step as in the drainage process. There was only one sharp increase of the water saturation.

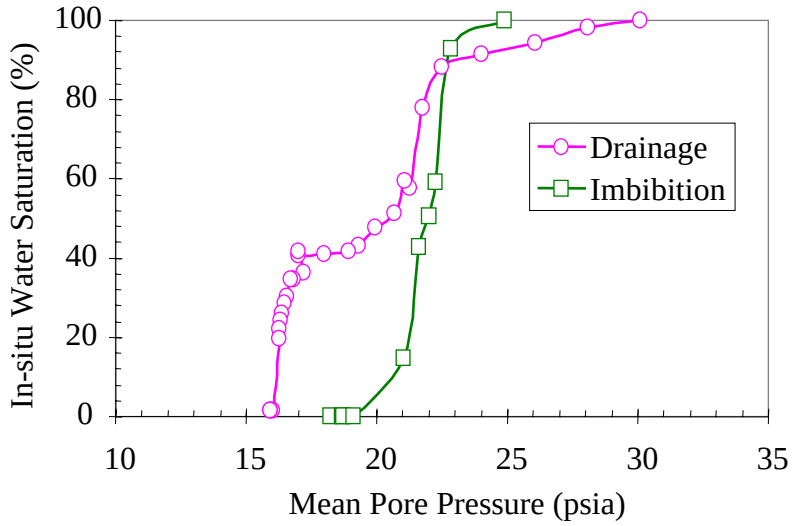

Figure 3.8: Effect of mean pore pressure on the in-situ water saturation.

According to the drainage curve in Figure 3.8, the water in the core sample started to boil at a pressure of about 28 psia, which is much greater than the saturation pressure (20.8 psia) at a temperature of 110^{o}C. This phenomenon may be due to the effect of capillary pressure. A question arises. Since the core sample is over 40 cm long, the water may boil in the region near the outlet even the mean pore pressure is greater than the saturation pressure. In order to exclude this possibility, the relationship between the water saturation and the absolute outlet pressure is plotted in Figure 3.9.

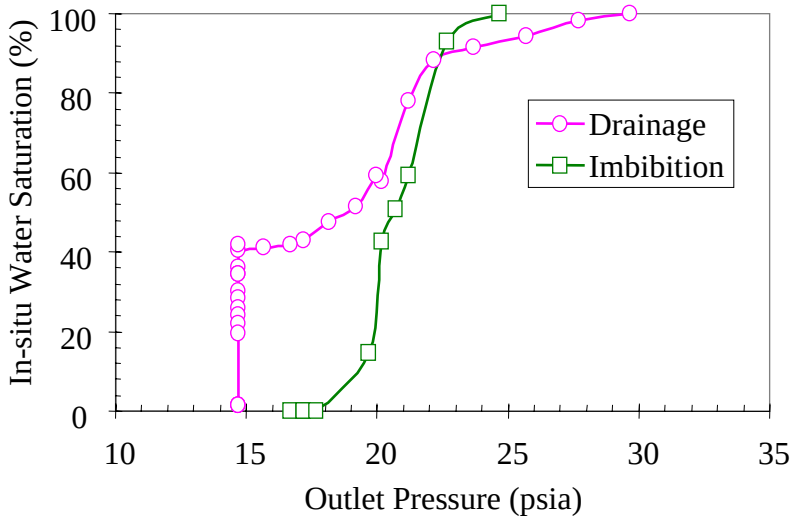

Figure 3.9: Relationship between in-situ water saturation and outlet pressure.

As observed in Figure 3.9, water in the core sample might boil when the outlet pressure was greater than the saturation pressure. Figures 3.8 and 3.9 show that water may start to

boil at a pressure much greater than the saturation pressure (20.8 psia in this experiment) in water-wet porous media. If the core were steam-wet, this would not happen.

After the imbibition, we decreased the temperature of the core system to about 94^{o}C in order to study the effect of temperature on the water saturation. The temperature was then raised gradually while the injection rate of water was kept at 0.5 ml/minute. The mean pore pressure was not constant during this process. The experimental data are shown in Figure 3.10. The water saturation decreased with the increase of temperature. There was a sharp drop of the water saturation at around 109^{o}C.

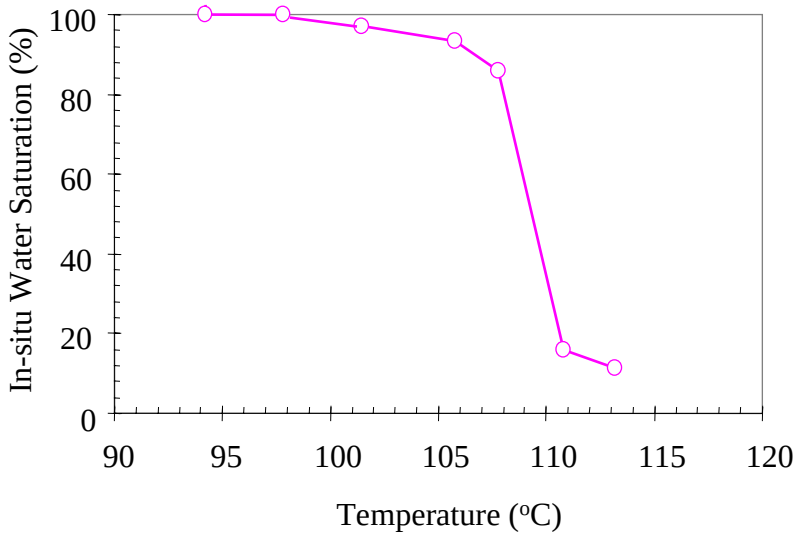

Figure 3.10: Effect of temperature on the in-situ water saturation.

The water injection rate influences the water saturation -- the higher the differential pressure, the greater the mean pore pressure. The experimental results are plotted in Figure 3.11. We can see that the in-situ water saturation increases with the increase of water injection rate.

Using the experimental data from the first drainage process (see Figure 3.8), we calculated the steam relative permeabilities at the water saturations under 40%. It was assumed that the water phase was immobile at these values of water saturation. The calculated results are shown in Figure 3.12.

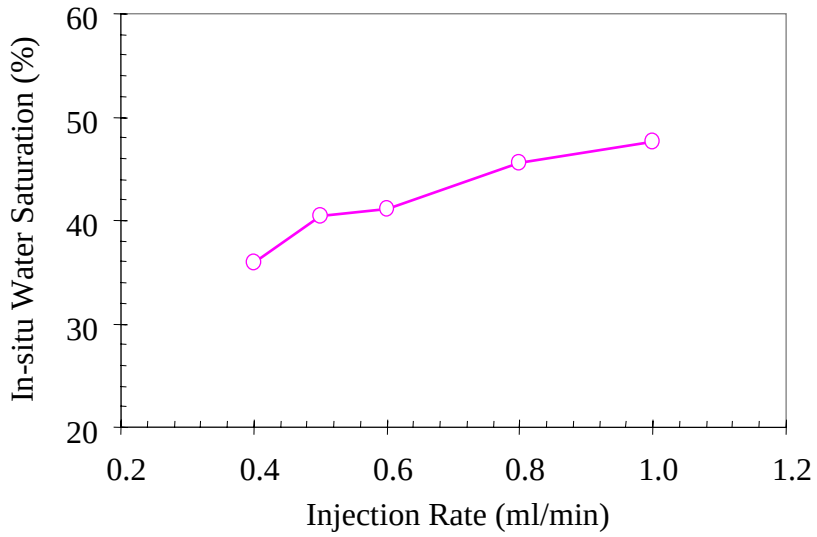

Figure 3.11: Effect of water injection rate on the in-situ water saturation.

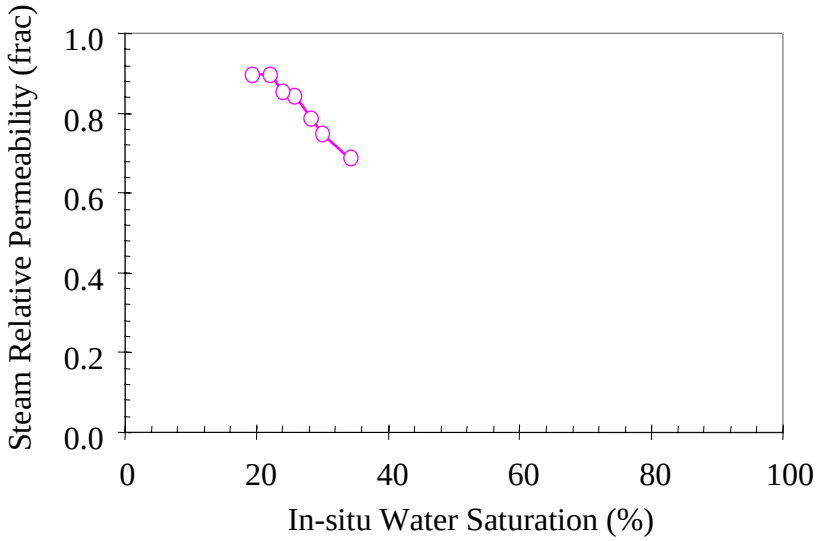

Figure 3.12: Steam relative permeabilities at a temperature of 110^{o}C.

The experimental data in Figure 3.8 were also used to calculate the productivity index represented by Eq. 3.2. The results are shown in Figure 3.13. The productivity index, in the unit of kg/Mpa.hr, increases with the increase of mean pore pressure and reaches a maximum value at a pressure close to the saturation pressure in both drainage and imbibition.

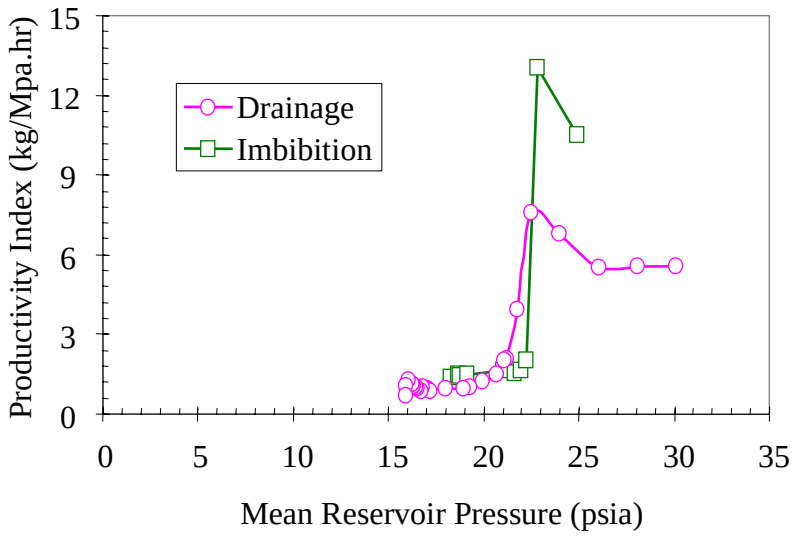

Figure 3.13: Effect of mean pressure on the productivity index.

It would be interesting to calculate the productivity index using the unit of liter/Mpa.hr. However, there is a difficulty to obtain the fraction of steam or water in the two-phase flow region so this calculation was not done.

3.6 CONCLUSIONS

Based on the present work, the following conclusions may be drawn:

1. An experimental method to model the water injection into geothermal systems and to measure end-point steam relative permeabilities has been developed.
2. The in-situ water saturation is dependent on the mean pore pressure and changes very sharply at a pressure close to the saturation pressure during both drainage and imbibition.
3. The in-situ water saturation increases with the increase of water injection rate and with the decrease of temperature.
4. The productivity index, in the unit of kg/Mpa.hr, increases with the increase of mean pore pressure and reaches a maximum value at a pressure close to the saturation pressure in both drainage and imbibition.
5. Water may boil at a pressure greater than the saturation pressure in water-wet porous media due to the effect of capillary pressure.

3.7 FUTURE WORK

We may conduct a similar experimental study using geothermal rocks.

4. INFERRING RESERVOIR CONNECTIVITY BY WAVELET ANALYSIS OF PRODUCTION DATA

This project is being conducted by Research Assistant Brian A. Arcedera and Prof. Roland Horne. The objective is to determine reservoir connectivity by applying wavelet analysis to data gathered in day-to-day operations. Use of this technique would establish the degree of connectivity between wells without doing additional tests and data gathering.

4.1 BACKGROUND

In 1998, Sullera used wavelet analysis and multiple regression techniques to infer injection returns by analyzing injection rates and chloride concentrations. The study indicated that wavelet analysis could isolate short-term signal variations which could be correlated from one well to another. The results of Sullera's study were verified successfully against tracer test data and qualitative field observations.

Sullera's study, however, only yielded successful results in one set of field data. Other data sets analyzed did not have sufficient data points for meaningful statistical correlations. The frequency of chloride data further hindered the approach by limiting the analysis to the use of monthly data. Data with monthly frequency may not be suitable for this analysis because they would not capture the short-term variations in the signal.

This project was conceived as an extension of Sullera's study. The study addresses the problems of lack of data and low sampling frequency by analyzing production data (e.g. total rate, steam rate, brine rate, wellhead pressure, enthalpy). Production data is already gathered on a regular basis for normal operating records so no additional tests or data gathering needs to be done.

4.2 METHODOLOGY

The analysis required in the study can be broken into four main steps: preprocessing, wavelet analysis, cross-correlation analysis, and multiple regression analysis.

The preprocessing step rearranges the data from different sources into a uniform format for subsequent analysis. Each data set from a unique source goes through a custom translation that extracts the pertinent information and writes it into a new file. This uniform data format is essential in the automation of the succeeding filtration and analysis steps. The formatted data is then filtered to remove nonnumeric entries and interpolated linearly to produce data signals over a uniform time interval. Safeguards in the interpolation macro prevent interpolation over long periods of missing data. In these cases, the data signal is truncated to include only the longest relevant time period.

The processed data signal is separated into a general approximation and a series of signal fluctuations through wavelet decomposition. Wavelet analysis separates the data into small sections and fits a predetermined wavelet function to each subgroup. Each level of wavelet decomposition handles a different section length thus capturing signal variations

at different time scales. Wavelet analysis is done using the Haar wavelet (a wavelet similar to a square wave) since it best captures the fluctuations expected from the on/off variations in surface conditions. This decomposition is applied until the approximation curve becomes smooth.

The different detail signals obtained in the wavelet analysis from different wells are analyzed in groups to determine correlations between them. Different types of production data are paired and analyzed in turn (e.g. injection rate – production enthalpy, or injection rate – production wellhead pressure). For each pair of data type, cross-correlation is done for each detail level between wells to determine any signal lag so that the data can be adjusted accordingly.

The adjusted signals can be analyzed through multiple regression to determine the effects of one data signal on another. For each pair of wells being analyzed, the different detail levels will be compared and the regression coefficients noted. The detail level with the best meaningful correlation will be analyzed further. The regression parameters obtained at the best detail level will be compared to other well pairs to infer relative connectivity strengths between them. Figure 4.1 illustrates the process workflow.

4.3 CONTINUING WORK

The wavelet analysis was applied initially to a group of relatively isolated injection wells. Injection wells were chosen to test the analysis procedure because of the availability of daily injection data. By comparison, production data from the Tiwi geothermal field is recorded in intervals of five to nine days, which would require further data preparation. Another reason for choosing the group of injection wells was to determine if surface connectivity effects through pipelines could be isolated from reservoir connectivity effects.

Three injection wells were processed through the wavelet decomposition procedure: Nag-08, Nag-70, and Nag-71. Figure 4.2 shows the decomposition of the injection rate data for Nag-70. The figure shows the original signal, *s*, followed by the approximation, a_8, and the different detail levels, d_n, all plotted against the number of days elapsed since February 1, 1990. The wavelet analysis separates the general trend (shown in a_8 as a declining injection rate for this particular well), and gives us the detail signals indicating fluctuations over different time intervals. These fluctuations are what we hope to correlate between wells and ultimately use to determine reservoir connectivity.

The date of data acquisition was masked by indexing the data by the number of days elapsed since the date of the first available data for that well. This was done to provide a one-dimensional data set that could be manipulated more easily through wavelet analysis. The signal offset for the three injector wells was determined as a check on the cross-correlation function that is used to determine lag time. Since a common injection network supplies the injectors, it is expected that there will be no lag time. The signal offset provided by the cross-correlation should then give us the date difference between the first

available data of each well upon which the elapsed time is based. In fact, the results from the cross-correlation gave us the exact date differences expected.

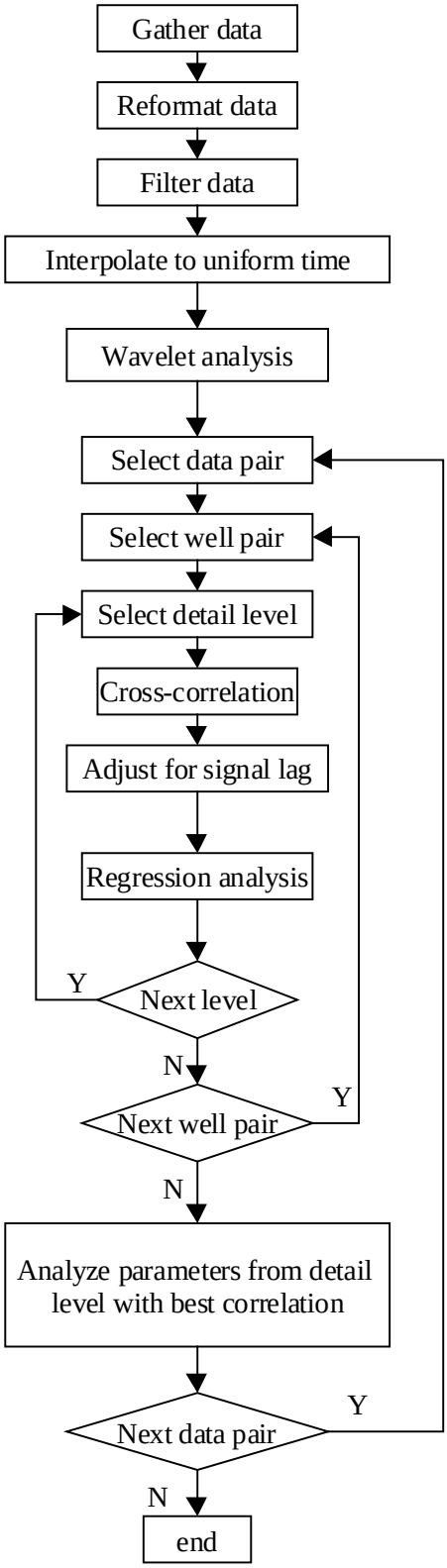

Figure 4.1: Simplified process workflow.

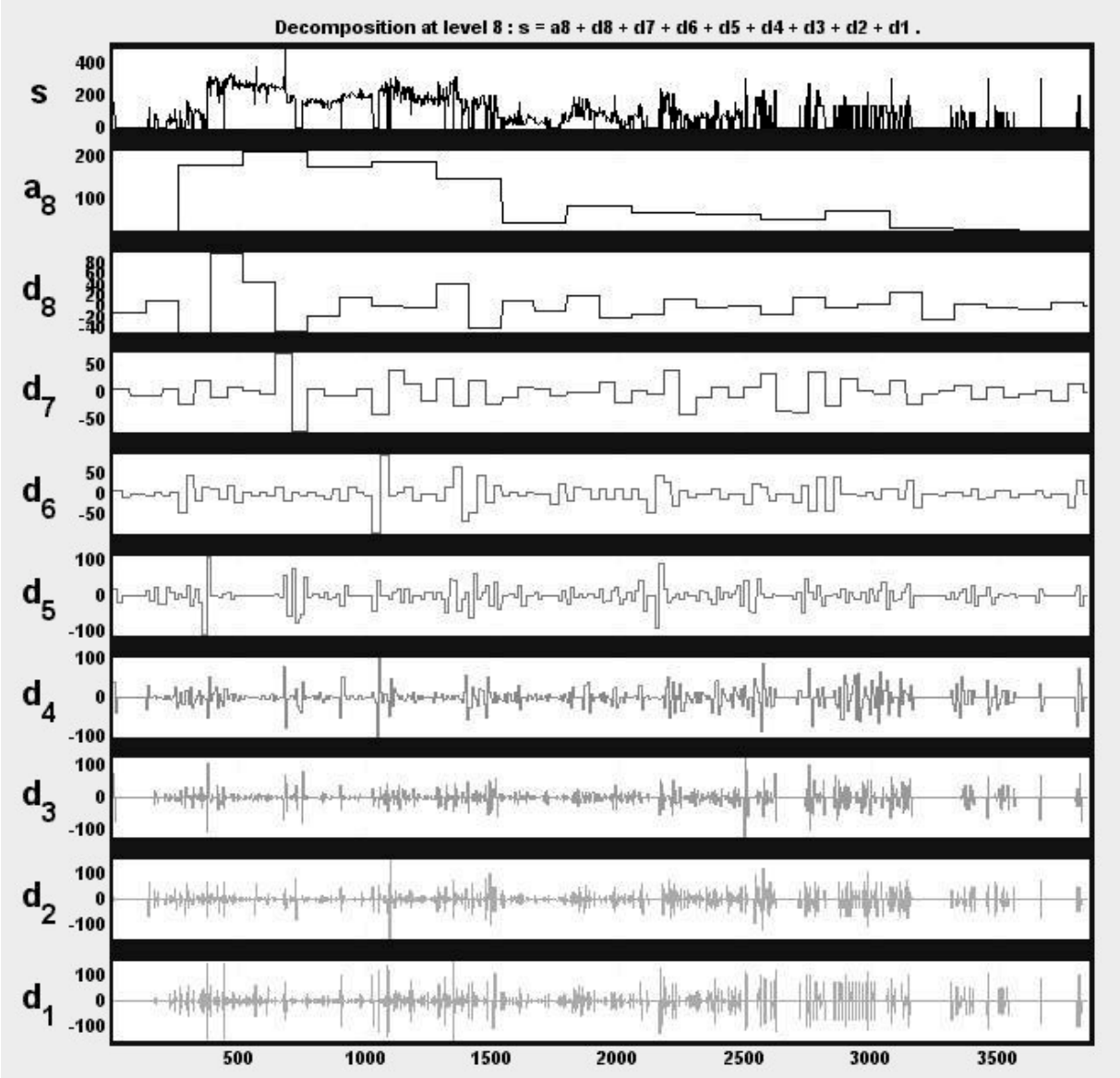

Figure 4.2: Wavelet decomposition of Nag-70 daily injection data. Note: x-axis represents number of days since 1 February 1990.

Figure 4.3 compares the injection rate from the three injectors. The wells are all tied-in to one injection network and, as expected, exhibit strong data correlation resulting from their surface connections. This surface connectivity might be isolated from the signal through wavelet decomposition. Figure 4.4 compares the details signal (d1) of the three wells over a data frequency of one day. Visual inspection of the plots leads us to assume that this detail level captures the data correlation. A comparison of the details signal from the three wells over a data frequency of 1 month (d6) is shown in Figure 4.5. Visual inspection of the plots at this frequency seems to show a better correlation between the latter two wells – Nag-70 and Nag-71. However, statistical tools will still be used to better evaluate the correlation.

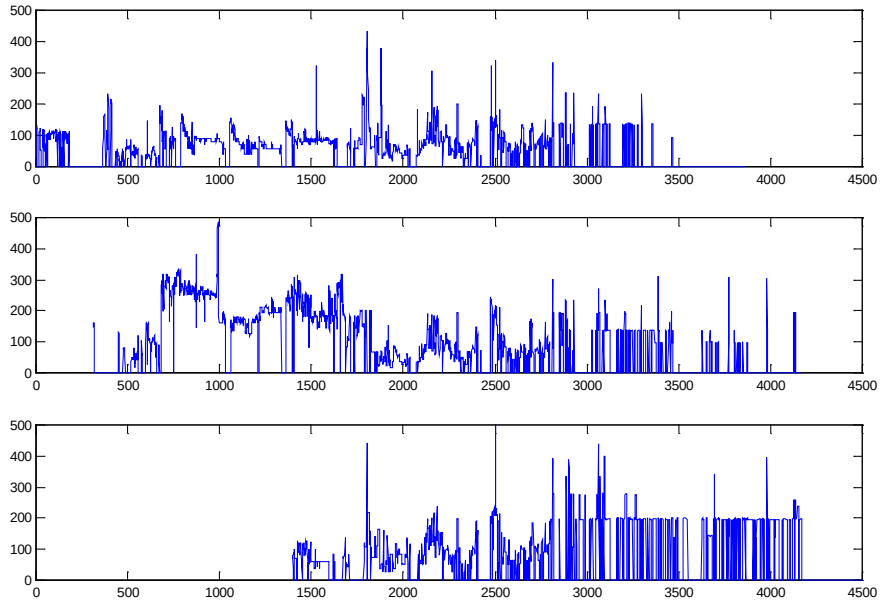

Figure 4.3: Injection rate (x1000 lbs/hr) plotted against number of days elapsed since March 26, 1989 (from top to bottom: Nag-08, Nag-70, and Nag-71).

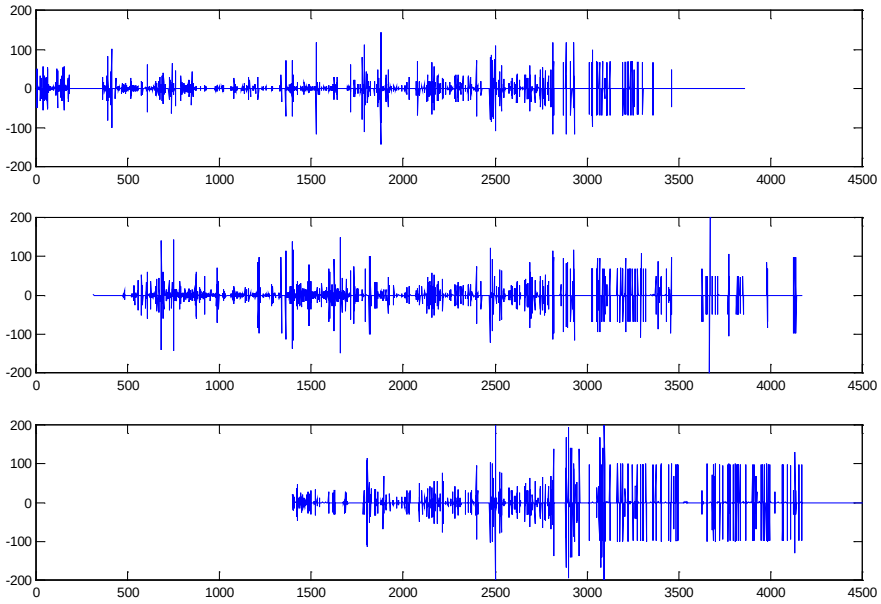

Figure 4.4: Detail level 1 (daily frequency) of injection rate (x1000 lbs/hr) plotted against number of days elapsed since March 26, 1989 (from top to bottom: Nag-08, Nag-70, and Nag-71).

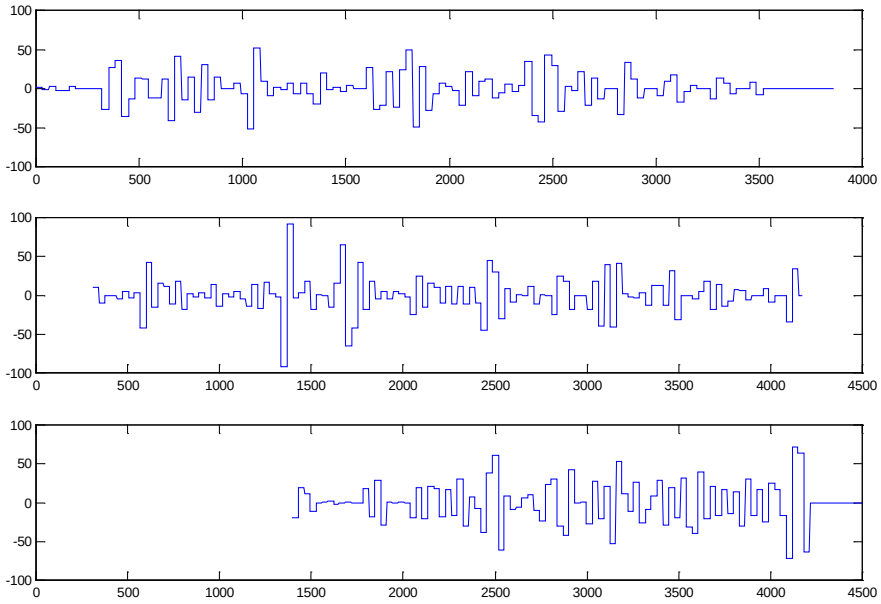

Figure 4.5: Detail level 6 (~monthly frequency) of injection rate (x1000 lbs/hr) plotted against number of days elapsed since March 26, 1989 (from top to bottom: Nag-08, Nag-70, and Nag-71).

Analysis of the three injection wells illustrates that our procedures for using wavelet analysis to decompose the production data into an approximation and a series of detail levels at different frequencies can be applied properly. The next step in our analysis will be to use statistical tools to interpret reservoir connectivity from the detail signals. Basic statistical tools can be used to determine quantitatively which of the signals in Figure 4.5 are really more closely correlated.

After the initial testing of our procedures, production and injection data will be analyzed. In particular, we will be looking at data from the Tiwi and MakBan geothermal fields in the Philippines. The first data pairs analyzed will be injection rate against production wellhead pressure, and injection rate against production enthalpy. It is hoped that analyzing these data pairs will provide information on injection returns in these specific fields. In particular, information on the effects of injection returns in the form of pressure support as well as effects on reservoir enthalpy may prove useful.

5. EXPERIMENTAL INVESTIGATION OF STEAM AND WATER RELATIVE PERMEABILITY ON SMOOTH WALLED FRACTURE

This project is being conducted by Research Assistant Gracel P. Diomampo, Research Associate Kewen Li and Prof. Roland Horne. The goal is to gain better understanding of steam-water flow through fractured media and determine the behavior of relative permeability in fractures.

5.1 BACKGROUND

Geothermal reservoirs are complex systems of porous and fractured rocks. Complete understanding of geothermal fluid flow requires knowledge of flow in both types of rocks. Many studies have been done to investigate steam and water flow through porous rocks, however fewer studies have examined multiphase flow in fractures. Only a few published data are available most of which have been done for air-water or for water-oil systems. Earliest is Romm's (1966) experiment with kerosene and water flow through an artificial parallel-plate fracture lined with strips of polyethylene or waxed paper. Romm found a linear relationship between permeability and saturation, $S_w = k_{rw}$, $S_{nw} = k_{rnw}$ such that $k_{rw}+k_{rnw} = 1$. Pan et al. (1996) performed a similar experiment with an oil-water system but arrived at conflicting results -- significant phase interference was observed such that $k_{rw} + k_{rnw} < 1$. Both studies, however, concluded that residual saturations are zero and that a discontinuous phase can flow as discrete units along with the other phase.

In an attempt to develop a relationship between fracture relative permeability and void space geometry, Pruess and Tsang (1990) conducted numerical simulation for flow through rough-walled fractures. Their study showed the sum of the relative permeabilities to be less than 1, residual saturation of the nonwetting phase to be large, and phase interference to be greatly dependent on the presence or absence of spatial correlation of aperture in the direction of flow. Persoff et al. (1991) performed experiments on gas and water flow through rough-walled fractures using transparent casts of natural fractured rocks. The experiments showed strong phase interference similar to that seen in the flow in porous media. The data of Persoff (1991) and Persoff and Pruess (1995) for flow through rough-walled fractures were compared in Horne et al. (2000), as shown in Figure 5.1.

Presently, the mechanism of flow and the characteristic behavior of relative permeability in fractures are still undetermined. As yet unresolved are issues such as whether a discontinuous phase can travel as discrete units carried along by another phase or will be trapped as a residual saturation as in porous media. The question of phase interference is still unanswered, i.e. whether the curve of relative permeability vs. saturation is an X-curve, Corey curve, or some other function. The main objective of this study is to contribute to the resolution of these issues. Experiments using air-water flow through smooth-walled fractures will be done first with the aim of establishing a reliable methodology for flow characterization and permeability calculation. Then these experiments will be repeated with steam-water flow; and with rough-walled fractures.

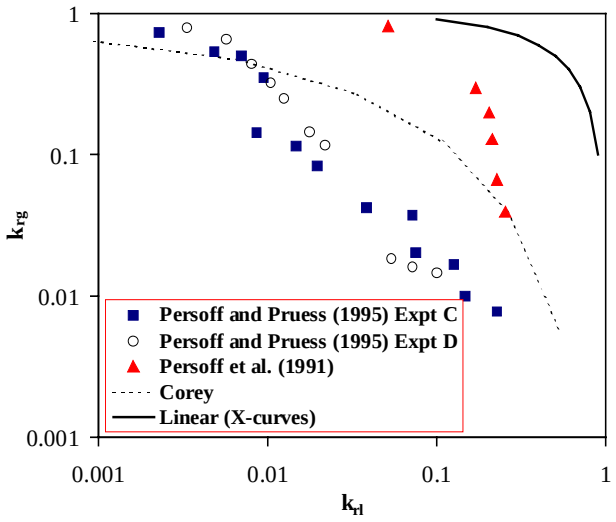

Figure 5.1: Some measurements of air-water relative permeabilities in rough-walled fractures (graph from Horne et al. (2000))

5.2 EXPERIMENTAL APPARATUS AND MEASUREMENT TECHNIQUES

The smooth-walled fracture apparatus consisted of a 183 cm by 31 cm horizontal glass plate on top of an aluminum plate. The aperture between the glass and aluminum plates was dictated by 0.2-mm thick shims inserted between them. The shims were placed along the boundaries and in three columns along the flow area. It should be noted that the shims placed as columns along the plate did not divide the plate into separate flow sections. This was deduced upon observing cross flow along the shims.

The sides of the plates were sealed together with silicone adhesive. Even with the adhesive, the inlet head had to be kept below 15 cm to avoid leakage. This constraint presented a maximum limit in the flow rates approximately 2 cc/sec for water and 9 cc/sec for nitrogen.

Horizontal slits at the ends of the metal plate served as entry and exit points for the fluids. There were two available canals for input of gas and liquid. The options to inject nitrogen and water as separate streams or as mixed fluid in a single stream were tried. It was found that mixing the gas and water prior to input caused no significant improvement in fluid distribution. Thus, the gas and water streams were injected separately for simplicity, ease of flow rate control, and inlet pressure reading.

Gas flow was controlled through a flow regulator. A meter pump controlled the rate of liquid injection. Dye was dissolved in the injection reservoir for better phase identification. Figure 5.2 shows a schematic diagram of this configuration.

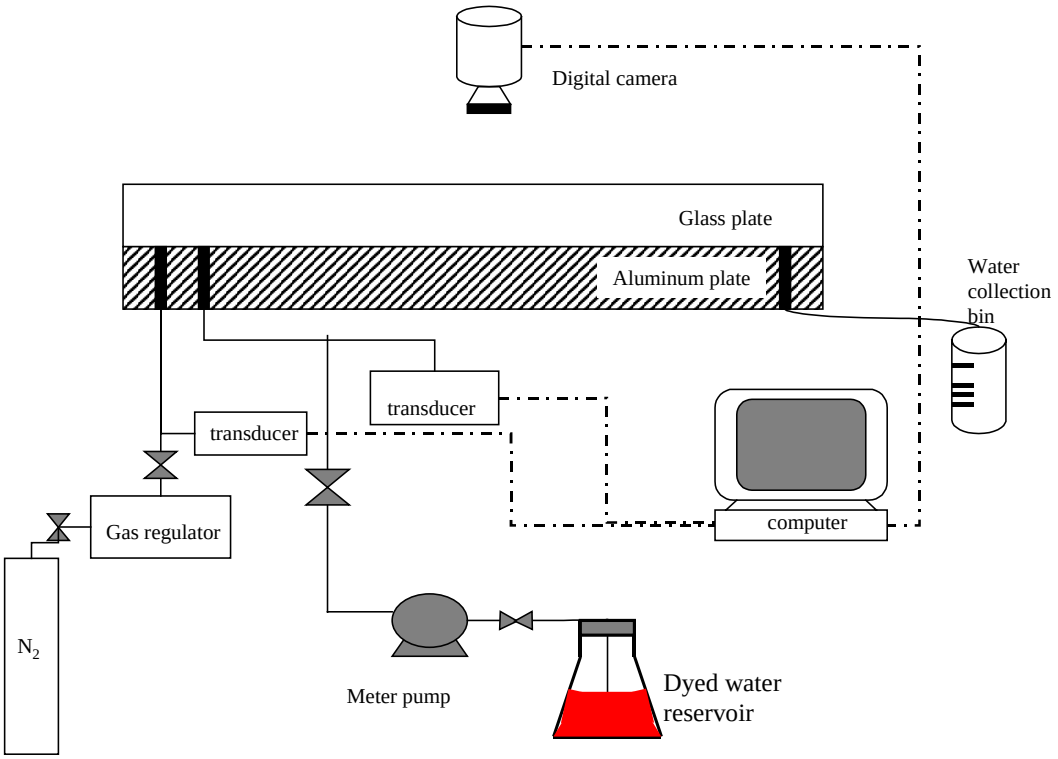

Figure 5.2: Experimental set-up for air and water flow through smooth walled fractures.

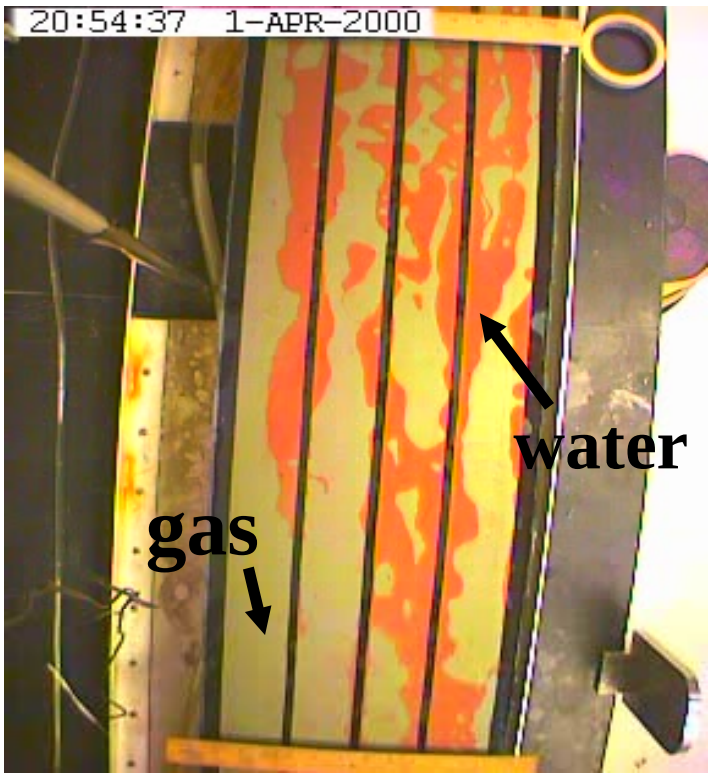

Figure 5.3: Sample camera image for two-phase run.

Low capacity transducers measured the gas and liquid inlet pressures separately. These transducers were attached to a Labview program designed to record data at user-specified time intervals. The water rate was read from the pump meter and gas rate from the regulator. Saturation was computed by measuring the area that each phase occupied. This was done by taking digital photographs of a constant area of the plate at a particular gas and water rate. The area was around 3 ft. long and was chosen far enough from the ends of the plates to avoid end effects. Figure 5.3 shows a sample photo from a two-phase run. The photographs were processed in a Matlab program. The program uses quadratic discriminant analysis to group the pixels of the photograph into three groups: the water phase, gas phase, and the shim. The grouping was based on color differences. Saturation was calculated as total pixels of liquid group over the sum of the gas and liquid group. Figure 5.4 is a comparison of the gray-scale image produce by the program and the original photograph from the digital camera. The accuracy of the program in calculating the saturation can be confirmed from the similarity in details of the gray-scale image to the true image. From the figure, it can be said that the program has reasonable accuracy.

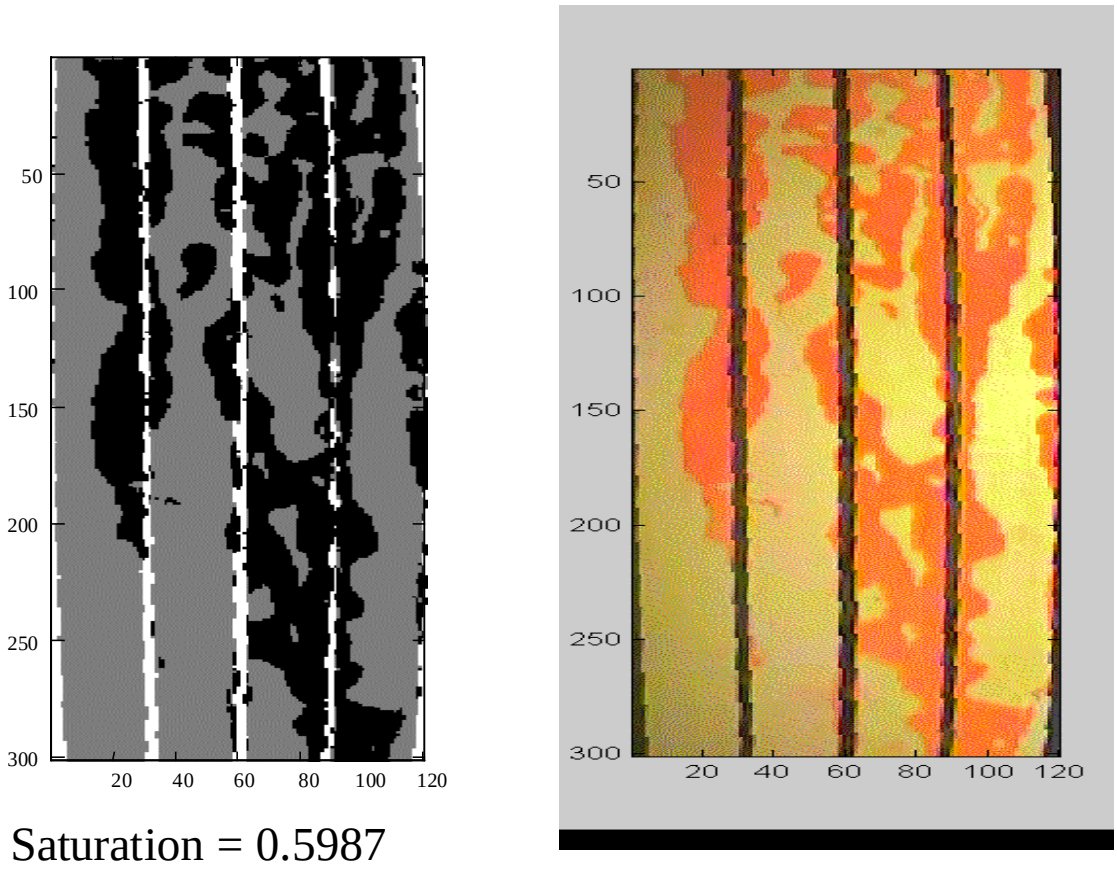

Figure 5.4: Comparison of gray-scale image produced by the Matlab program to actual photo taken by digital camera.

Pan et al. (1996) also used this technique for measurement of saturation. This study noted that the sources of error in this technique were the quality of the photographs and the water film adsorbed on the surfaces of the plates with the latter being of minimal effect. Good quality photographs are the ones with clear distinction between the gas and

liquid phases. The use of dyed liquid enhanced visualization of phase boundaries and produced better quality photographs.

5.3 PARTIAL RESULTS AND DISCUSSION

Preliminary experiments were done with q_{gas}/q_{liq} values of 1, 5, 10, 20 and single-phase runs at residual saturation. There were some important observations:

In these ratios of q_{gas}/q_{liq}, the water and gas phase traveled along the plate as separate channels. These separate flow paths changed with time and position. This is illustrated in the series of images in Figure 5.5, which were taken at constant gas and liquid rate. This observation implies that at these ratio, phases move individually and not as "moving islands" or "globules" of the discontinuous phase carried along by the other phase. It also suggests that there is no local steady-state saturation.

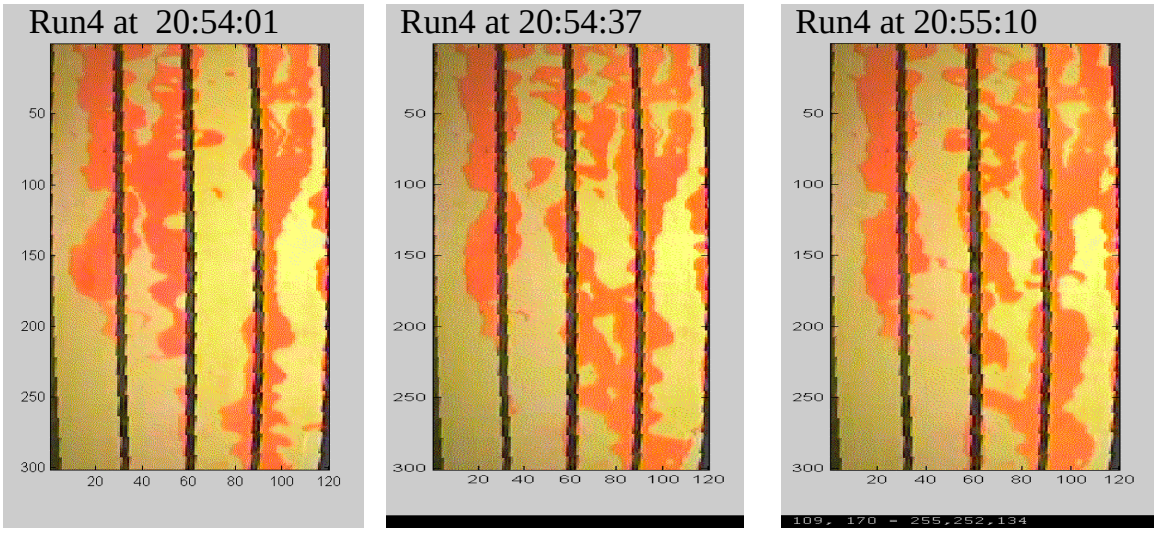

Figure 5.5: Images at constant gas and liquid rate in short time intervals to illustrate changes in the gas and liquid flow paths.

These fast changes in flow paths were accompanied by pressure fluctuations. When the gas established enough energy to break through the water flow path, there was a corresponding increase in inlet gas pressure and decrease in water line pressure. The same was true when the water phase breaches through gas channels. This fluctuation caused difficulty in registering the current pressure.

Residual saturations obtained were very low. Residual water saturation S_{wr} was around 0.02 -0.06. Similarly, residual steam saturation S_{gr} was around 0.04-0.06. This indicates that there is negligible trapping in this smooth-walled fracture.

Pan et al. (1996) discussed two approaches in data analysis: the porous medium approach where Darcy's law is used and the homogeneous single-phase approach where the system

is treated as a single-phase pipe flow. Because of the observations in the experiments, it seemed appropriate to treat the data using porous medium approach.

Darcy's law was used to obtained the single-phase and two-phase liquid permeability:

$$k_l = \frac{q_i \mu L}{(p_i - p_o)} \tag{5.1}$$

subscripts 'o' stands for outlet and 'i' for inlet, μ the viscosity, p as pressure, L for length of the plate and q as Darcy flow velocity from

$$q_o = \frac{Q_o}{bw} \tag{5.2}$$

where Q is the volumetric rate, b the aperture and w as the width of the plate.

The relative permeability is then calculated by taking the ratio of the two-phase k_l with the single-phase k_l.

The gas permeability was calculated using the equation from Scheidegger (Scheidegger, 1974):

$$k_g = 2q_o \mu L \frac{p_o}{p_i^2 - p_o^2} \tag{5.3}$$

Similarly, taking the ratio of the two-phase k_g with single-phase run gives the relative permeability.

The complete list of calculated relative permeability values, their corresponding saturation range is shown in Table 5.1. Figures 5.6 and 5.7 show plots of these data along with the X-curves. The data are clustered over a small saturation range and lie far from the X-curves.

5.4 FUTURE WORK

Further experiments with nitrogen-water system will be done at higher orders of variation of q_{gas}/q_{liq}. This will be to obtain wider saturation range in the relative permeability curves. To investigate the flow mechanism further, a digital video camera will be used to record the flow. A voltmeter has been attached to the transducer and its pressure reading will be recorded visually along with the flow. Snapshots will be taken from the video recording. These snapshots will be analyzed to observe the periodic snap-off and reconnection of flow channels, pressure fluctuations and accompanying changes in saturation.

The experiment will also be performed with sand or glass beads in between the glass and aluminum plate to simulate flow through rough-walled fractures.

Simultaneous with these nitrogen-water experiments, design of a similar apparatus for steam-water system is under study. The challenges encountered in the design include:

(a) keeping the whole system isothermal at high temperature while maintaining safety and good visibility of flow, (b) acquiring accurate steam-water flow rate measurements, and (c) achieving a wide saturation range at flow rates that give detectable pressure drops.

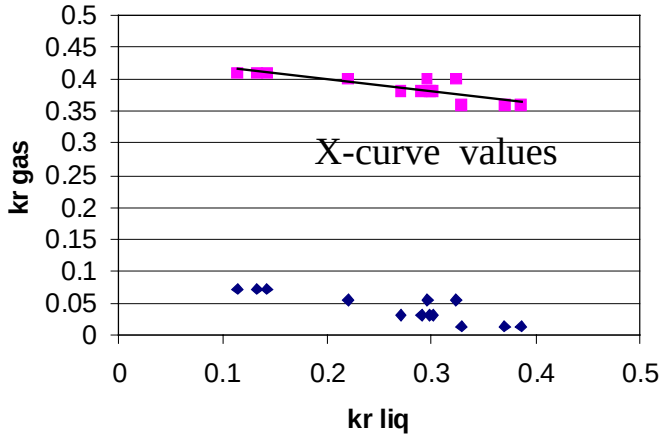

Figure 5.6: Comparison of experimental relative permeability values with X-curve values.

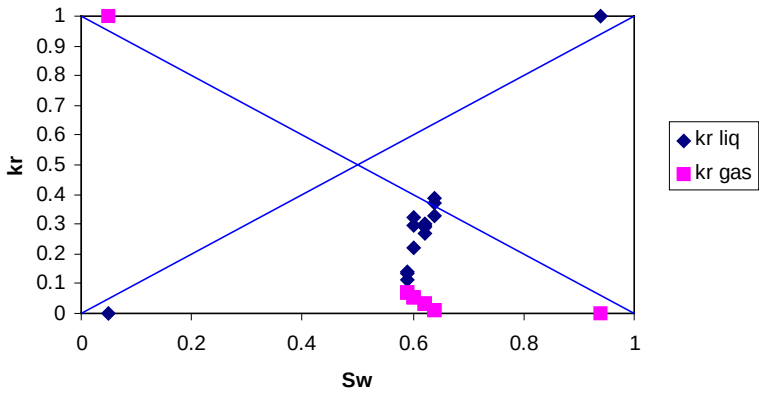

Figure 5.7: Experimental relative permeability values against saturation.

Table 5.1: Calculated relative permeability values.

run #	Qg	Gas Head	krg	Qw	Water Head	krl
	(cc/min)	(cm H2O)		(cc/min)	(cm H2O)	
1	74	12.5	0.013	35.16	11.5	0.385
1	74	12.5	0.013	33.77	11.5	0.370
1	74	12.5	0.013	29.97	11.5	0.328
2	172	13	0.030	26.51	11.5	0.291
2	172	13	0.030	27.45	11.5	0.301
2	172	13	0.030	27.19	11.5	0.298
3	172	13	0.030	24.71	11.5	0.271
3	332	13.7	0.055	26.98	11.5	0.296
3	332	13.7	0.055	29.51	11.5	0.323
3	332	13.7	0.055	20.04	11.5	0.220
4	407	12.8	0.072	12.36	11.0	0.142
4	407	12.8	0.072	9.92	11.0	0.114
4	407	12.8	0.072	11.52	11.0	0.132

6. REFERENCES

Hanselman, D. and Littlefield, B. *Mastering Matlab 5 A Comprehensive Tutorial and Reference*, Prentice-Hall, Inc.,New Jersey, 1998.

Horne, R.N., Satik, C., Mahiya, G., Li, K., Ambusso, W., Tovar, R., Wang, C., and Nassori, H.: "Steam-Water Relative Permeability," *Proc*. of the World Geothermal Congress 2000, Kyushu-Tohoku, Japan, May 28-June 10, 2000.

Li, K. and Horne, R.N. (2000a): "Steam-Water Capillary Pressure," SPE 63224, presented at the 2000 SPE Annual Technical Conference and Exhibition, October 1-4, 2000, Dallas, TX, USA.

Li, K. and Horne, R.N. (2000b): "Characterization of Spontaneous Water Imbibition into Gas-Saturated Rocks," SPE 62552, presented at the 2000 SPE/AAPG Western Regional Meeting, Long Beach, California, 19–23 June 2000.

Li, K. and Horne, R.N. (2000c): "Steam-Water Capillary Pressure in Geothermal Systems," presented at the 25th Stanford Workshop on Geothermal Reservoir Engineering, January 24-26, 2000, Stanford University, Stanford, CA 94043, USA.

Mahiya, G.F.: *Experimental Measurement of Steam-Water Relative Permeability*, MS report, Stanford University, Stanford, Calif., 1999.

Pan, X., Wong, R.C., and Maini, B.B.: "Steady State Two-Phase Flow in a Smooth Parallel Fracture", presented at the 47th Annual Technical Meeting of the Petroleum Society in Calgary, Alberta, Canada, June 10-12, 1996.

Persoff, P., and Pruess, K.: "Two-Phase Flow Visualization and Relative Permeability Measurement in Transparent Replicas of Rough-Walled Fractures", Proceedings, 16th Workshop on Geothermal Reservoir Engineering, Stanford University, Stanford, CA, Jan. 23-25, 1991, pp 203-210.

Pruess, K., and Tsang, Y. W.: "On Two-Phase Relative Permeability and Capillary Pressure of Rough-Walled Rock Fractures", *Water Resources Research* **26** (9), (1990), pp 1915-1926.

Satik, C.: "A Study of Steam-Water Relative Permeability", paper SPE46209 presented at the SPE Western Regional Meeting, 10-13 May 1998, Bakersfield, California.

Scheidegger, A.E. *The Physics of Flow Through Porous Media*, 3rd ed., University of Toronto, Toronto. 1974.

Sullera, M.M., and Horne, R.N.: "Inferring Injection Returns from Chloride Monitoring Data", to appear in *Geothermics, 2000.*